Editors' Suggestion

# Three-dimensional imaging of integrated-circuit activity using quantum defects in diamond

Marwa Garsi,[1,2,*] Rainer Stöhr,[1] Andrej Denisenko,[2] Farida Shagieva,[2] Nils Trautmann,[3] Ulrich Vogl,[3] Badou Sene,[4] Florian Kaiser,[1,†] Andrea Zappe,[1] Rolf Reuter,[1] and Jörg Wrachtrup[1]

[1] *Third Institute of Physics, IQST, and Research Center SCoPE, University of Stuttgart, 70569 Stuttgart, Germany*
[2] *Solid State Quantum Technologies, TTI GmbH, 70569 Stuttgart, Germany*
[3] *Corporate Research and Technology, Carl Zeiss AG, Carl-Zeiss-Straße 22, 73447 Oberkochen, Germany*
[4] *Mobility Electronics, Robert Bosch GmbH, 72762 Reutlingen, Germany*

(Received 11 September 2023; accepted 18 December 2023; published 29 January 2024)

The continuous scaling of semiconductor-based technologies to micrometer and submicrometer regimes has resulted in higher device density and lower power dissipation. Many physical phenomena such as self-heating or current leakage become significant at such scales, and mapping current densities to reveal these features is decisive for the development of modern electronics. However, advanced noninvasive technologies either offer low sensitivity or poor spatial resolution and are limited to two-dimensional spatial mapping. Here we use near-surface nitrogen-vacancy centers in diamond to probe Oersted fields created by current flowing within a multilayered integrated circuit in predevelopment. We show the reconstruction of the three-dimensional components of the current density with a magnitude down to about $\approx$10 μA/μm$^2$ and submicrometer spatial resolution at room temperature. We also report the localization of currents in different layers and observe anomalous current flow in an electronic chip. Our method therefore provides a decisive step toward three-dimensional current mapping in technologically relevant nanoscale electronics chips.

DOI: 10.1103/PhysRevApplied.21.014055

## I. INTRODUCTION

The rapid growth and downscaling of silicon integrated circuits (ICs) have ushered revolutions in many areas of today's society [1–4], such as high-speed internet [5], in-car navigation [6] and leadless pacemakers [7]. However, if the semiconductor community has underpinned Moore's law [8] for over 50 years by shrinking the size of electronic components, the scaling roadmap is nearing its end [1,9]. As a result, next-generation technologies such as autonomous driving [10] and quantum processors [11] rely on a new strategy: three-dimensional chip architectures [12–16]. In this regard, device development, optimization and failure analysis are severely challenged due to the absence of methods for direct visualization of three-dimensional charge flow. This particularly concerns multilayer chips with submicrometer feature sizes.

Most electric current imaging techniques visualize charge transport through the associated magnetic fields that pass unaffected through the materials used in semiconductor devices. One approach involves delayering the chip to probe fields with a microneedle [17]. Although this technique enables high spatial resolution, it inherently alters the current path. Nondestructive current imaging can be implemented using superconducting quantum interference device (SQUID) microscopes, but the inherent standoff distance limits the spatial resolution to tens of micrometers [18]. Alternatively, giant magnetoresistance (GMR) microscopes provide excellent spatial resolution but come at the expense of much lower field sensitivities [19,20]. However, SQUID and GMR microscopes are only sensitive to a single magnetic field component, limiting reliable current imaging to the two-dimensional realm.

In this article, we demonstrate current imaging in a three-dimensional IC using quantum sensors at room temperature. We use nanoscale nitrogen-vacancy (N-*V*) centers in diamond [21,22] which offer the ability to probe all three vectorial components of a magnetic field simultaneously at the nanoscale [23,24] and in a noninvasive fashion. Besides, N-*V* centers operate under a wide span of external conditions [25–29] and demonstrate excellent sensitivity to magnetic fields [30,31].

Pioneering work has successfully demonstrated current imaging at the nanoscale [32,33] and IC activity imaging [34–36] with N-*V* centers but has so far been restricted to two-dimensional current imaging. In this work, we

*m.garsi@pi3.uni-stuttgart.de
†Now at Luxembourg Institute of Science and Technology (LIST).

 

demonstrate three-dimensional current distribution imaging within a microchip designed with the recent back-end-of-line (BEOL) technology [13,37]. For this, we employ an N-$V$-based wide-field microscope, described in Fig. 1(a), to synchronously map vectorial magnetic fields over a region of 90 μm × 90 μm. We use the instrument to measure the current density flow in the multilayered IC [Fig. 1(b)], notably without using prior knowledge about its design during the analysis process.

## II. CURRENT DENSITY IMAGING USING N-$V$ CENTERS

The principle of the experiment is depicted in Fig. 1(c). Long-range magnetic fields, also known as Oersted fields, are created by moving charges according to the Biot-Savart law given by

$$\mathbf{B}(\mathbf{r}) = \frac{\mu_0}{4\pi} \iiint \frac{\mathbf{J}(\mathbf{r}') \times (\mathbf{r} - \mathbf{r}')}{|\mathbf{r} - \mathbf{r}'|^3} d^3 r, \tag{1}$$

where $\mu_0$ is the vacuum permeability, $\mathbf{r}$ represents the spatial coordinates at the observation point, and $\mathbf{J}(\mathbf{r}')$ is the current distribution in the source plane.

The magnetic field isolines in Fig. 1(c) show that magnetic field contributions merge with distance from the current source, resulting in blurry patterns. In our experiment, we place a diamond homogeneously implanted with near-surface N-$V$ centers in the vicinity of the current flow, at only a few hundred nanometers from the surface of the IC. The electron spin of each N-$V$ center is thus affected by the magnetic field via the Zeeman interaction $\mathcal{H}_{\rm EZ} = -\gamma_{\rm N\text{-}V} B \cdot S$ where $\gamma_{\rm N-V}$ is the N-$V$-associated electron spin gyromagnetic ratio, $\mathbf{B}$ is the total magnetic field in the vicinity of the N-$V$ center and $\mathbf{S}$ represents the spin operators for the electron spin with $S = 1$.

Probing this Zeeman interaction on the multiple N-$V$ orientations, naturally occurring in the diamond lattice [Fig. 1(d)], is done by performing optically detected magnetic resonance (ODMR) on the N-$V$ centers [24] (see Supplemental Material [38]). We inject a total current $I = 19.8$ mA into the circuit which splits into several subpaths, creating distinct local Zeeman shifts on the ODMR spectra [Fig. 1(e)]. For each pixel of our image, we fit the spectrum to extract the eight resonance frequencies. Finally, we compare the extracted resonance frequencies to the ground-state N-$V$ spin Hamiltonian, including the zero-field splitting, the Zeeman and the Stark effects (see Supplemental Material [38]).

We perform the experiment on two distinct chips labeled as device 1 and device 2. Investigation of both samples

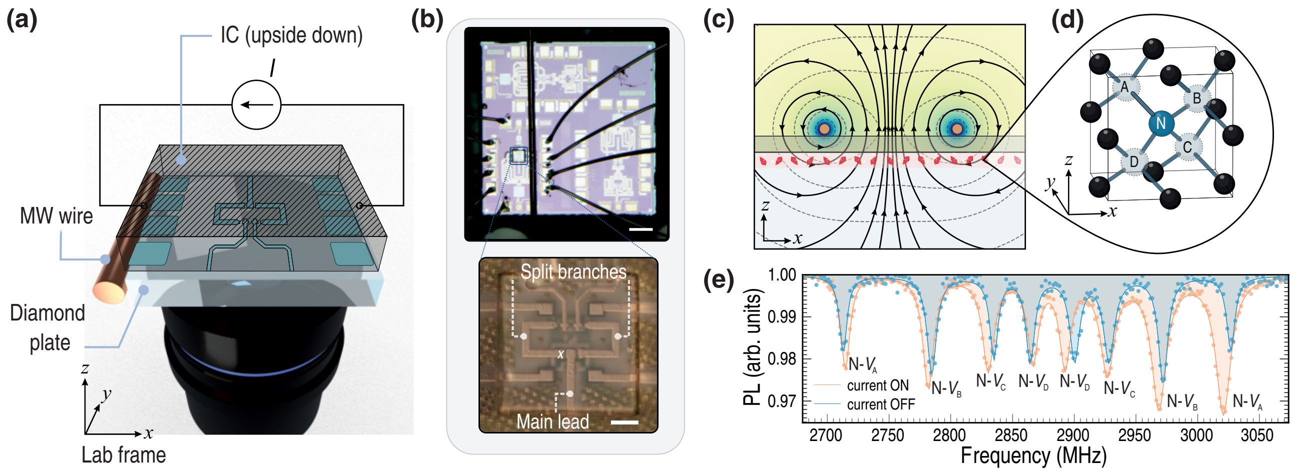


FIG. 1. Mapping integrated circuit (IC) activity with quantum sensors. (a) Schematic of the experiment. A microfabricated diamond plate contains a layer of near-surface N-$V$ centers and is glued to an integrated circuit. The sample is mounted to an inverted microscope where laser and microwave (MW) radiations excite the N-$V$ centers. A charge coupled device camera records the emitted photoluminescence (PL). (b) Photograph of the IC microchip. The top picture shows the overall chip with different circuit designs. The diamond plate is glued to a region of interest outlined by a blue square. A copper wire carrying MWs is placed next to the diamond, and wire bonds connect the chip to a power supply. The bottom picture shows a zoom-in on the diamond plate. Scale bars are 200 μm for the top photograph and 20 μm for the bottom one. (c) Visualization of the cross-section of the experiment. The current-carrying wires generate Oersted fields sensed by a layer of N-$V$ centers represented in red and separated by a protective overcoat from the leads. Solid lines with arrows represent the magnetic flux lines, and dashed lines represent magnetic field isolines. (d) Representation of the four possible tetrahedral orientations of the N-$V$ bond (A, B, C, D) in the $x$-$y$-$z$ reference frame. (e) ODMR spectra from a single pixel near the edge of a semiconductor stripe indicated by the white cross in (b). The blue spectrum is obtained with a bias magnetic field $B_0$ used to split the eight resonances lines of the N-$V$ ensemble. The orange spectrum is acquired when current flows in the IC, creating a shift in the resonances due to the Zeeman interaction of the N-$V$ centers with the Oersted field. Solid lines are multiple-Lorentzian fits. Each resonance is labeled according to the corresponding N-$V$ orientation, defined in (d).

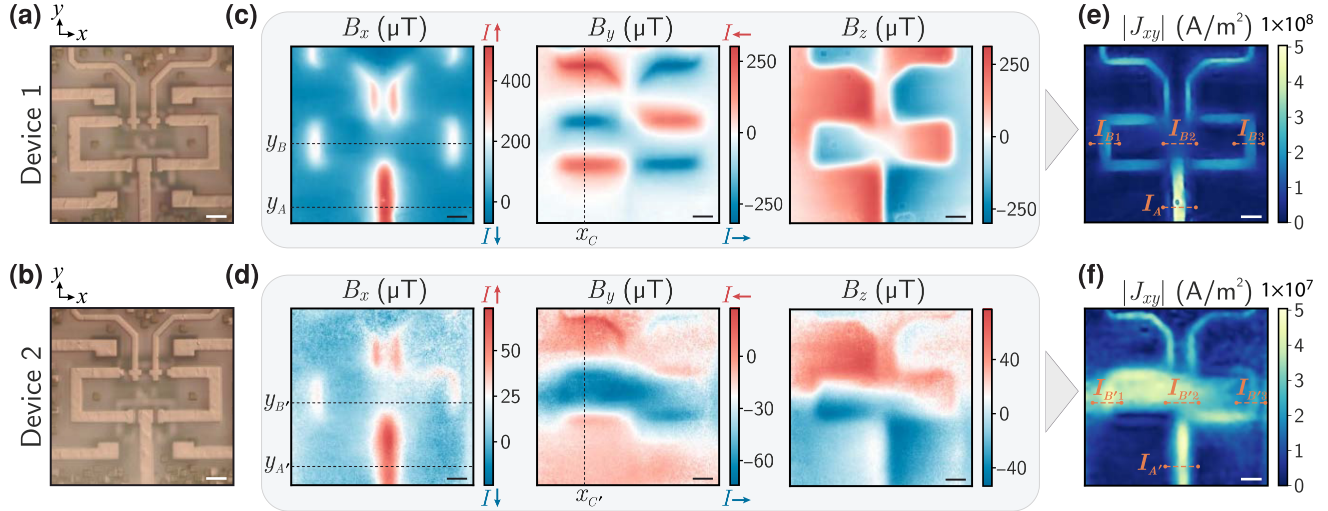


FIG. 2. Vectorial magnetic field produced by the current-carrying wires: device 1 versus device 2 and corresponding current density maps. (a),(b) Optical images of device 1 and device 2, respectively. (c),(d) Mapping of the three vectorial magnetic field components $B_x$, $B_y$, $B_z$ produced by the operational and defective IC, respectively. The sign gives the direction of the field. Linecuts at $y_A$, $y_{A'}$, $y_B$, $y_{B'}$ are shown in Figs. 3(b) and 3(c) for further analysis. Linecuts at $x_C$, $x_{C'}$ are shown in the Supplemental Material [38]. (e),(f) Corresponding in-plane current density map reconstructed from $B_x$ and $B_y$ in (a) and (b) respectively. The orange labels indicate the sections where the current amplitudes in Fig. 3 are estimated. Scale bars are 10 μm.

under light microscopy [Figs. 2(a) and 2(b)] reveals no difference. On the contrary, mapping the Oersted fields exposes a failure immediately. With device 1, Fig. 2(c) shows Oesterd fields clearly reflecting the geometry of the underlying structure. In Fig. 2(d), we can see that device 2 produces nearly one order of magnitude lower magnetic fields [a maximum amplitude of $|B_x| = 513(6)$ μT compared to 73(5) μT]. Furthermore, the magnetic field patterns $B_y$ and $B_z$ produced by device 2 exhibit a mismatch with those produced by device 1. Thus, comparing the magnetic field produced by the two devices can already help identify anomalous behavior given the high dynamic range of the N-$V$ centers.

To better understand the current distribution producing such Oersted field patterns, we reconstruct the lateral current density $J_{xy}$. We follow the procedure described in Refs. [39,40] and use the components of the magnetic field $B_x$ and $B_y$ to numerically invert the Biot-Savart law [Eq. (1)], resulting in the lateral current density $|J_{xy}|$ shown in Figs. 2(e) and 2(f) (see Supplemental Material [38]). It is important to note that since the magnetic field signals are collected outside the device to perform a nondestructive measurement, all the fields generated in different layers merge, resulting in a flattened image. This characteristic makes nondestructive imaging of three-dimensional ICs difficult and, thus, testing and validation of modern chips challenging [41]. In Fig. 2(e), the current paths in device 1 follow the shape of the visible structure shown in Fig. 2(a). A closer look at the central part of the map reveals a weak current contribution with wide lateral spreading, indicating that additional currents flow underneath. Finally, the flow appears weaker in some parts of the circuit, such as at the sharp corners. We can see in Fig. 2(f) that several current sources produce fields of similar intensity in device 2. Observing $|J_{xy}|$ alone, without further information about the field distribution over the vertical axis $z$, is insufficient to comprehend the current path.

In Sec. III, we investigate the different layer contributions to locate the flow within the device and in Sec. IV, we seek the third dimension of the current density, $J_z$.

## III. LOCALIZATION OF CURRENTS INSIDE A MULTILAYERED DEVICE

To resolve the signal in the vertical direction $z$, we investigate different linecuts along $x$ in the magnetic field map $B_x$ (Fig. 3). We fit the linecuts with the Biot-Savart model [Eq. (1)], using the infinite-wire approximation [Eq. (2)],

$$B_{x,y} = \frac{\mu_0 I_{y,x} \Delta z}{2\pi[|r_{xy} - r_{\text{wire}}|^2 + \Delta z^2]} + o, \tag{2}$$

where $I_{y,x}$ is the lateral current amplitude, $r_{xy}$ represents the observation position on the $xy$-plane, $r_{\text{wire}}$ the position of the current source on the $x$-$y$ plane, $\Delta z$ is the distance between the current source and the observation position on the vertical axis $z$, and $o$ is a constant offset [Fig. 3(a)].

The fitting procedure reveals a contribution from two layers: the first at $\Delta z_1 = 4.5(5)$ μm away from the layer of N-$V$ centers, and the second at $\Delta z_2 = 8.5(8)$ μm (see Supplemental Material [38]). These distances are validated by comparison with the actual values, estimated at $\Delta z_{1,\text{true}} = 4.5(1)$ μm and $\Delta z_{2,\text{true}} = 7.9(1)$ μm. For device 1

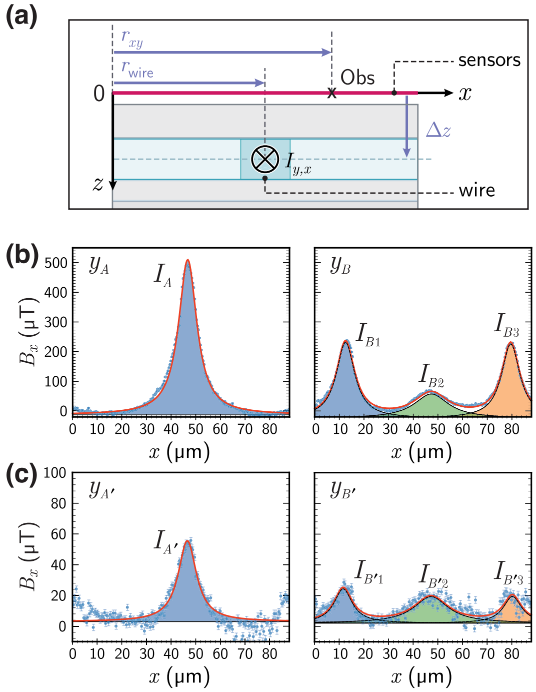


FIG. 3. Experimental contributions of Oersted fields originating from different layers. (a) Schematic view of the $x$-$z$ plane of the experiment. The variables used to fit the data with Eq. (2) are labeled according to an arbitrarily chosen observation point Obs. (b) Linecuts of experimental data (blue dots) outlined in Fig. 2(c) along the $x$-axis at a vertical position $y_A$ (left panel) and at a vertical position $y_B$ (right panel). The fit (solid red line) returns a current amplitude of $I_A = 11.77(6)$ mA where the source-sensor distance is fixed at $\Delta z_A = 4.5$ μm for the left panel and current amplitudes of $I_{B1} = 5.64(5)$ mA, $I_{B2} = 3.49(8)$ mA, $I_{B3} = 5.76(5)$ mA where the source-sensor distances are fixed at $\Delta z_{B1,B3} = 4.5$ μm and $\Delta z_{B2} = 8.5$ μm for the right panel. (c) Linecuts of experimental data (blue dots) outlined in Fig. 2(d) along the $x$-axis at a vertical position $y_{A'}$ (left panel) and at a vertical position $y_{B'}$ (right panel). The fit (solid red line) returns a current amplitude $I_{A'} = 1.18(4)$ mA where the source-sensor distance is fixed at $\Delta z_{A'} = 4.5$ μm for the left panel and current amplitudes of $I_{B'1} = 0.50(3)$ mA, $I_{B'2} = 0.73(5)$ mA, $I_{B'3} = 0.39(3)$ mA where the source-sensor distances are fixed at $\Delta z_{B'1,B'3} = 4.5$ μm and $\Delta z_{B'2} = 8.5$ μm for the right panel. Error bars correspond to one standard deviation. Plain colors underline the contribution of each single wire.

(device 2), we identify a current of amplitude $I_A$ ($I_{A'}$) in the main lead, dividing into currents of amplitude $I_{B1}$ ($I_{B'1}$) and $I_{B3}$ ($I_{B'3}$) in the split branches [Figs. 3(b) and 3(c)]. By referring to the expected values of direct current in the main lead and the split branches given by the manufacturer, we can conclude that the device 2 presents a failure. When comparing the results from device 2 (defective) to device 1 (operating), most of the loss appears on the outer layer (at $\Delta z_1$), presenting one order of magnitude lower current amplitude. In contrast, the deeper layer (at $\Delta z_2$) presents a smaller loss. Finally, the analysis of other line profiles reveals another current contribution at $\Delta z_2$ present in the operating and defective devices, in both cases with no apparent anomaly (see Supplemental Material [38]). From these observations, we conclude that failure happens in the layer at $\Delta z_2$ and then affects the outer layer by propagation.

Overall, the simple model with infinite-wire approximation already shows excellent agreement with the experimental data. In order to verify the consistency of the procedure, we now perform a simulation of Oersted fields produced by a multilayered device. The simulation reproduces the layering of the chip, derived from a SiGe technology described in Ref. [37], the sensor-device geometry, and some of the apparent geometric features of the chip for guidance only.

The total thickness of the simulated structure is 11.8 μm and combines 12 stacked layers [Fig. 4(a)]. As depicted in Fig. 4(b), two layers across the structure are electrically active and labeled as first and second active layer (AL). Through-silicon vias (TSVs) connect the first AL to the bottom layer of the structure. We investigate magnetic fields generated by this structure, resulting in patterns at the position of the sensors shown in Fig. 4(c). Similarly to the experimental observations (Fig. 2), the contribution from the first AL is clearly defined and unambiguously related to the shape of the structure. The contribution from the second AL shows a pronounced lateral spreading, and the signal arising from two distinct wires starts to blur out. Finally, the contribution from the vertical current is weak due to both the observation position and the presence of counterpropagating flows which average out magnetic field contributions (see Supplemental Material [38]). Still, a current propagating vertically has a nonzero contribution in $B_{xy}$ compared to its contribution in $B_z$ (see Supplemental Material [38]). Therefore, currents propagating in the $z$ direction can be sensed by N-$V$ centers contrary to magnetometers such as SQUID and GMR sensors since they only measure the out-of-plane component of the magnetic field $B_z$. These magnetometers indirectly identify vertical currents by monitoring a discontinuity in the current path. However, interpreting the current discontinuity can be difficult to interpret since signals produced by counterpropagative sources can cancel each other. Besides, as further discussed in the Supplemental Material [38], analyzing signals from multilayered devices is more reliable with N-$V$ centers since there is no ambiguity in identifying orthogonal overlapping signals.

Lastly, to study the flow in the three-dimensional structure and observe vertical currents, we can infer information about the third component of the current density, $J_z$.

## IV. THREE-DIMENSIONAL CURRENT DENSITY MAPPING

The current-carrying wires have a nonnegligible thickness of a few hundred nanometers, leading to a possible

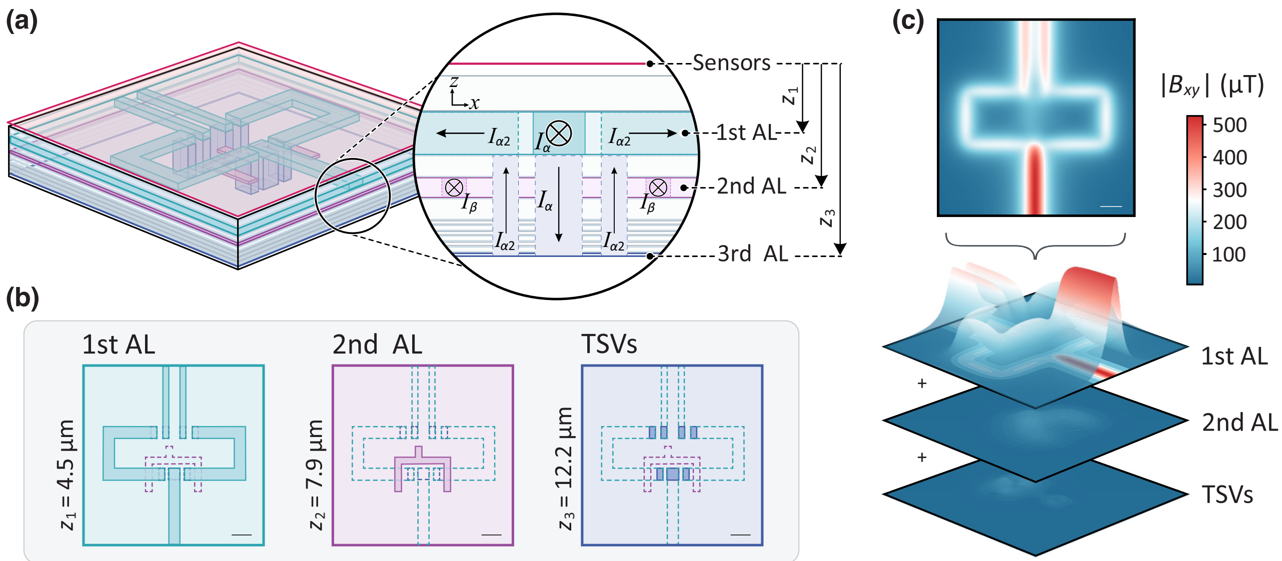


FIG. 4. Simulation of Oersted field contributions originating from different layers. (a) Geometry of the simulated structure. A layer of N-$V$ centers is separated from the chip by 0.8 µm. The structure is composed of 12 layers comprising the two ALs and TSVs. A current of amplitude $I_\alpha = 11.8$ mA goes to the main branch of the first AL, flows down to the bottom layer of the structure where it splits into two subpaths with an amplitude of $I_{\alpha 2} = I_\alpha/2$ and flows back to the first AL. In the second AL, a current of amplitude $I_\beta = 2$ mA is injected into each of the two branches which combine to a single one afterwards. (b) Top view of each AL of the structure. The first AL, second AL, and the bottom layer of the structure are located at $z_1 = 4.5$ µm, $z_2 = 7.9$ µm and $z_3 = 12.2$ µm respectively from the sensors. (c) *Top*: Oersted field in the $x$-$y$ plane generated by all active components at the sensors layer position. *Bottom*: Separate contribution from each AL where the vertical axis shows the lateral magnetic field amplitude $|B_{xy}|$.

contribution of the current's $z$-component. In order to evaluate the total current density in all directions, we now consider a component $J_z \neq 0$ in Eq. (1) (see Supplemental Material [38]). The resulting maps are shown in Figs. 5(a)–5(c) and the results suggest three-dimensional contribution of the current flow inside the wires. It is important to note that the maps shown in Figs. 5(a)–5(c) still represent a signal where all the contributions over the vertical axis $z$ are merged. Using the fitting algorithm employed in Fig. 3 over the entire map would enable the

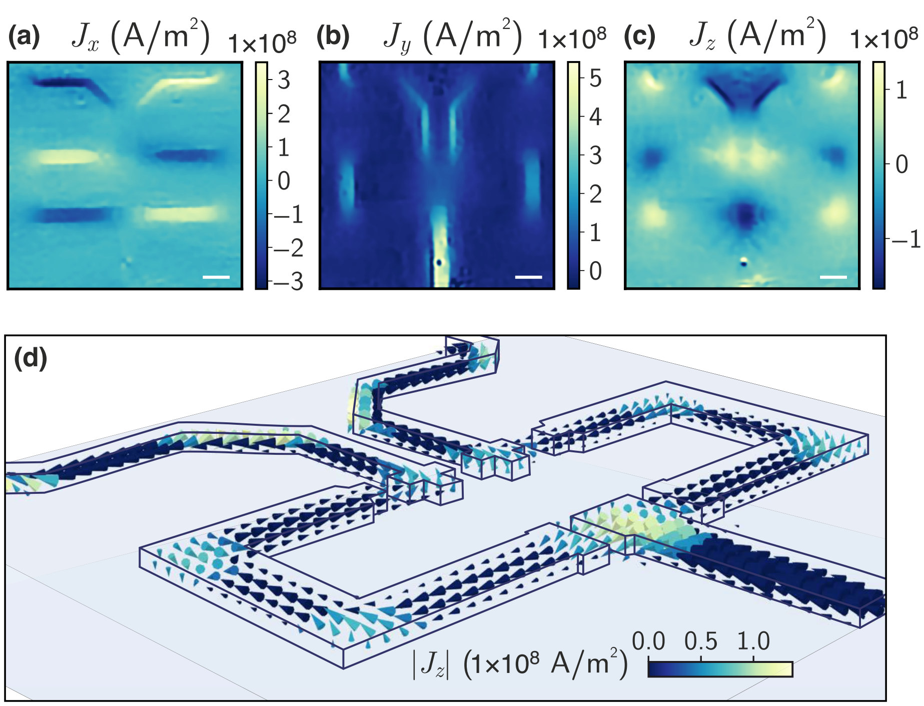


FIG. 5. Current density maps. (a)–(c) Images of the three vectorial components of the current density $J_x$, $J_y$, $J_z$ for device 1. Scale bars are 10 µm. (d) Three-dimensional representation of the current flow in the outer layer of the IC. The thickness of the arrow scales with the total current density magnitude and the color scales with the magnitude of $J_z$.

selection of the signal from each layer separately. However, the layout must be known for devices thick of several micrometers to reconstruct the current density reliably over the entire chip since the magnetic field spreading from the deep layers is too prominent. Thus, in Fig. 5(d), we only represent the current in the outer lead for visualization. In Figs. 5(c) and 5(d) we can see a nonnegligible current flow in the $z$-direction at the edges and the corners of the leads. Thus, using a two-dimensional model for a three-dimensional device can lead to locally underestimating the current amplitude. For example, a weaker current density was observed at the corners of the split branches when considering a lateral flow only (Fig. 2). This information can be crucial for evaluating current crowding at corners in interconnect structures, which plays an essential role in nucleating voids and hence failure of ICs [42–44].

More importantly, having access to the full-vector information of the current density helps quantify and understand the current flow through different stacks in layered materials. For instance, in the outer layer, we can observe a prominent $J_z$ contribution at the edge of the main lead. As for the simulation (Fig. 4), this contribution is the averaged result from counterpropagating currents in vias. Current in the main lead flows down to a deeper layer where it splits into two paths and goes back to the outer layer to further flow in the split branches (see Supplemental Material [38]). As the component $B_z$ does not carry information about $J_z$, and $B_{xy}$ shows a specific pattern with the presence of counterpropagating fields, developing an algorithm using $B_{xy} - B_z$ and pattern recognition techniques [45] is the next step to identify the contribution from each current source over the entire device.

## V. CONCLUSION

Using N-$V$ centers in diamond, we have demonstrated imaging of three-dimensional current density in a multilayered integrated circuit. First, we compared the current flow in two devices, primarily identical under light microscopy, and identified an operational chip and a defective one. Exploiting the N-$V$ center's high dynamic range, we observed one order of magnitude lower current amplitude in the defective device, which demonstrates its potential use for failure analysis of ICs. Furthermore, we have shown how to localize currents originating in different leads even with multiple stacked layers. Lastly, we have presented imaging of the three vectorial components of the current density. Although the out-of-plane component of the current density $J_z$ is generally neglected in current density imaging techniques, we revealed a significant out-of-plane contribution of $J_z$ close to sharp edges. Finally, we have discussed how to image three-dimensional current density over the entire device. In this regard, resolving currents from different sources across the structure depends on the spatial resolution of the imaging technique. N-$V$ centers offer the closest sensor-sample proximity known so far and can demonstrate spatial resolution of only a few tens of nanometers with a scanning probe setup [32]. However, the device's configuration, including the capping layer, limits the spatial resolution of the magnetic fields and, thus, of the current density maps. In order to nondestructively resolve each layer with higher resolution, one solution is to interpolate the current distribution at the source plane using additional layout information, which can be obtained directly using circuit designs or ptychographic x-ray laminography techniques [46].

Additionally, N-$V$ centers can be used to explore various magnetic field regimes [47–51] and can be operated with high-speed imaging [52,53]. Combining a practical N-$V$-based imager [54] with x-ray imaging [55] will provide complete information on nanoscale three-dimensional current-carrying structures [56]. Such an imager is thus particularly relevant for designing modern three-dimensional electronic chips where failure analysis is primordial to predict and determine the root cause of a malfunction and thus steer the manufacturing process adequately at an early stage [41].

Finally, unraveling three-dimensional electronic signals using N-$V$ centers will leverage further advancements in many areas. For instance, it will serve neuroimaging to overcome the limits of conventional current density imaging techniques and help to reveal new features [57]. The N-$V$-based microscope would serve to observe charge transport in diverse multilayered electronic systems in science and technology [58,59].

## ACKNOWLEDGMENTS

We gratefully acknowledge T. Rendler for valuable discussions and technical assistance. We acknowledge the support of the European Union's Horizon 2020 research and innovation program under Marie Skłodowska-Curie Grant Agreement No. 765267 (QuSCo) and Grant Agreement No. 820394 (ASTERIQS). This work was supported by the European Research Council via SMeL, the DFG via GRK 2642 and by the Fraunhofer Society via the project QMag.

## APPENDIX A: DIAMOND SUBSTRATE

The diamond plates are fabricated by combining electron-beam lithography and reactive ion plasma etching. Prior to fabrication, N-$V$ centers are created by implantation of nitrogen with an energy of 9.8 keV and an implantation dose of $2 \times 10^{12}$ cm$^{-2}$ into a 100-oriented chemical vapor deposition diamond (electronic grade, Element Six). After implantation, the diamond is annealed at 960 °C for 2 h at a pressure of $10^{-7}$ mbar. The resulting N-$V$ centers concentration is about of $2 \times 10^{10}$ cm$^{-2}$.

The depth distribution profile is nearly Gaussian, peaking at 15 nm below the surface and with a nonnegligible concentration in depth ranging from ïĄąeglig5 to 25 nm.

The plates used here are about 3 μm thick and 100 μm in size. First, a tiny drop of UV-curable glue is placed on the IC sample. The diamond with the array of plates is then brought into close proximity to the sample, with the N-*V* layer facing toward the sample. An individual plate is then broken out of the array using a sharp tungsten tip mounted to a micromanipulator. By optical inspection, it is confirmed that the plate has not flipped during this step, which means that the N-*V* layer is facing the IC. The UV-curable glue is hardened after the plate has been fine-positioned to its final location. Finally, the Areal confocal 3D probe (NanoFocus AG) is used to measure the sample's height profile, enabling us to estimate the thickness of the glue to 0.8(1) μm.

## APPENDIX B: OPERATIONAL AND DEFECTIVE DEVICES

The microchip used in this article is a millimeter-wave test circuit for automotive radar applications designed using the multilayered BEOL technology, developed and described by the manufacturer in Ref. [37]. A capping layer of about 2.3 μm protects the conductive layers. Adding the thickness of the glue as sample-sensor distance, we estimate the distance of the active layers to the N-*V* centers to $\Delta z_{1,\text{true}} = 4.5(1)\ \mu$m and $\Delta z_{2,\text{true}} = 7.9(1)\ \mu$m. Although the circuit serves as a frequency doubler working in the vicinity of 160 GHz (2 × 80 GHz), it can be probed in the dc regime to evaluate the current path. To this end, expected current amplitudes for different bias voltages are given in the Supplemental Material [38]. A complete characterization over the several bias voltages is monitored to define the operational device's functioning. Finally, comparing the experimentally extracted current amplitudes to the expected values enables us to assess the faulty behavior.

## APPENDIX C: EXPERIMENTAL SETUP AND MEASUREMENT

The N-*V* imaging setup is a custom-built wide-field fluorescence microscope similar to the one used in Refs. [24, 49]. The microscope consists of an air objective (Olympus MPLAPON 50×, NA = 0.95), a 650-nm long-pass filter (Omega), a 300-nm tube lens and a Cascade II:512 charged coupled device camera (512 × 512 pixels, Photometrics), resulting in an effective pixel width of about 192 nm on the object side. Experimental realization of continuous-wave ODMR data was achieved by exciting N-*V* centers with a 532-nm laser (Coherent) controlled with an acousto-optical modulator (Crystal Technology) and coupled into the optical path with a dichroic mirror (Semrock). Simultaneously, microwave radiations were generated using a microwave (MW) source (SMBV100A, Rhode & Schwarz) and amplified (100S1G4, Amplifier Research) before being sent to a 50-μm-thick copper wire. The resulting MW power sent to the wire was approximately 30 dBm. For all the measurements reported in the main text, the total continuous-wave laser power at the back aperture of the objective was about 90 mW. The camera settings were set to 2 × 2 pixel binning and the field of view was defined to be approximately 90 μm × 90 μm. For a single frame, the exposure time was set to $t_{\text{expo}} = 16$ ms and the frame transfer time was $t_{\text{frame}} = 42$ ms. A single ODMR spectrum was acquired within 189 s and repeated 100 times.

The IC chip was wire bonded to a printed circuit board (PCB) with 20-μm-thick gold wires. The PCB was electrically connected to a power supply (Hameg, Rhode & Schwarz) generating 3.3 V of supply voltage to run the chip and an additional 2 V bias was used to vary the total current in the main circuit.

All measurements were performed in an ambient environment at room temperature, under a bias magnetic field $|B_0| \approx 5.8$ mT generated using a permanent magnet thermally stabilized at a temperature of about 37 °C.


[1] M. M. Waldrop, The chips are down for Moore's law, Nat. News **530**, 144 (2016).

[2] Q. Xu, B. Schmidt, S. Pradhan, and M. Lipson, Micrometre-scale silicon electro-optic modulator, Nature **435**, 325 (2005).

[3] H. Iwai and S. Ohmi, Silicon integrated circuit technology from past to future, Microelectron. Reliab. **42**, 465 (2002).

[4] M. Riordan and L. Hoddeson, Crystal fire: The invention, development and impact of the transistor, IEEE Solid-State Circuits Newsl. **12**, 24 (2009).

[5] T. Berners-Lee, R. Cailliau, A. Luotonen, H. F. Nielsen, and A. Secret, The World-Wide Web, Commun. ACM **37**, 76 (1994).

[6] I. Skog and P. Händel, In-car positioning and navigation technologies – a survey, IEEE Trans. Intell. Transp. Syst. **10**, 4 (2009).

[7] N. Bhatia and M. El-Chami, Leadless pacemakers: A contemporary review, J. Geriatr. Cardiol. **15**, 249 (2018).

[8] G. E. Moore, Cramming more components onto integrated circuits, Reprinted from Electronics, volume 38, number 8, April 19, 1965, pp.114 ff, IEEE Solid-State Circuits Soc. Newsl. **11**, 33 (2006).

[9] D. Mamaluy and X. Gao, The fundamental downscaling limit of field effect transistors, Appl. Phys. Lett. **106**, 193503 (2015).

[10] P. Bhargava, T. Kim, C. V. Poulton, J. Notaros, A. Yaacobi, E. Timurdogan, C. Baiocco, N. Fahrenkopf, S. Kruger, T. Ngai, Y. Timalsina, M. R. Watts, and V. Stojanovic, in *IEEE Symposium on VLSI Circuits, Digest of Technical Papers* (2019), pp. C262–C263.

[11] J. Chow, O. Dial, and J. Gambetta, IBM Quantum breaks the 100-qubit processor barrier, IBM Res. Blog (2021).

[12] P. Gargini, F. Balestra, and Y. Hayashi, Roadmapping of nanoelectronics for the new electronics industry, Appl. Sci. **12**, 308 (2022).

[13] S. Salahuddin, K. Ni, and S. Datta, The era of hyper-scaling in electronics, Nat. Electron. **1**, 442 (2018).

[14] E. P. DeBenedictis, M. Badaroglu, A. Chen, T. M. Conte, and P. Gargini, Sustaining Moore's law with 3D chips, Computer **50**, 69 (2017).

[15] A. Lancaster and M. Keswani, Integrated circuit packaging review with an emphasis on 3D packaging, Integration **60**, 204 (2018).

[16] A. W. Topol, D. C. La Tulipe, L. Shi, D. J. Frank, K. Bernstein, S. E. Steen, A. Kumar, G. U. Singco, A. M. Young, K. W. Guarini, and M. Ieong, Three-dimensional integrated circuits, IBM J. Res. Dev. **50**, 491 (2006).

[17] H. Wang, D. Forte, M. M. Tehranipoor, and Q. Shi, Probing attacks on integrated circuits: Challenges and research opportunities, IEEE Des. Test. **34**, 63 (2017).

[18] L. E. Fong, J. R. Holzer, K. K. McBride, E. A. Lima, F. Baudenbacher, and M. Radparvar, High-resolution room-temperature sample scanning superconducting quantum interference device microscope configurable for geological and biomagnetic applications, Rev. Sci. Instrum. **76**, 053703 (2005).

[19] B. D. Schrag and G. Xiao, Submicron electrical current density imaging of embedded microstructures, Appl. Phys. Lett. **82**, 3272 (2003).

[20] A. L. Herrera-May, L. A. Aguilera-Cortés, P. J. García-Ramírez, and E. Manjarrez, Resonant magnetic field sensors based on MEMS technology, Sensors **9**, 7785 (2009).

[21] F. Jelezko and J. Wrachtrup, Single defect centres in diamond: A review, Phys. Status Solidi A **203**, 3207 (2006).

[22] M. W. Doherty, N. B. Manson, P. Delaney, F. Jelezko, J. Wrachtrup, and L. C. L. Hollenberg, The nitrogen-vacancy colour centre in diamond, Phys. Rep. **528**, 1 (2013).

[23] G. Balasubramanian, I. Y. Chan, R. Kolesov, M. Al-Hmoud, J. Tisler, C. Shin, C. Kim, A. Wojcik, P. R. Hemmer, A. Krueger, T. Hanke, A. Leitenstorfer, R. Bratschitsch, F. Jelezko, and J. Wrachtrup, Nanoscale imaging magnetometry with diamond spins under ambient conditions, Nature **455**, 648 (2008).

[24] S. Steinert, F. Dolde, P. Neumann, A. Aird, B. Naydenov, G. Balasubramanian, F. Jelezko, and J. Wrachtrup, High sensitivity magnetic imaging using an array of spins in diamond, Rev. Sci. Instrum. **81**, 043705 (2010).

[25] A. Batalov, V. Jacques, F. Kaiser, P. Siyushev, P. Neumann, L. J. Rogers, R. L. McMurtrie, N. B. Manson, F. Jelezko, and J. Wrachtrup, Low temperature studies of the excited-state structure of negatively charged nitrogen-vacancy color centers in diamond, Phys. Rev. Lett. **102**, 195506 (2009).

[26] S. Steinert, F. Ziem, L. T. Hall, A. Zappe, M. Schweikert, N. Götz, A. Aird, G. Balasubramanian, L. Hollenberg, and J. Wrachtrup, Magnetic spin imaging under ambient conditions with sub-cellular resolution, Nat. Commun. **4**, 1607 (2013).

[27] J. Happacher, D. A. Broadway, J. Bocquel, P. Reiser, A. Jimenéz, M. A. Tschudin, L. Thiel, D. Rohner, M. L. G. Puigibert, B. Shields, J. R. Maze, V. Jacques, and P. Maletinsky, Low-temperature photophysics of single nitrogen-vacancy centers in diamond, Phys. Rev. Lett. **128**, 177401 (2022).

[28] G. Q. Liu, X. Feng, N. Wang, Q. Li, and R. B. Liu, Coherent quantum control of nitrogen-vacancy center spins near 1000 kelvin, Nat. Commun. **10**, 1344 (2019).

[29] M. Lesik, T. Plisson, L. Toraille, J. Renaud, F. Occelli, M. Schmidt, O. Salord, A. Delobbe, T. Debuisschert, L. Rondin, P. Loubeyre, and J. F. Roch, Magnetic measurements on micrometer-sized samples under high pressure using designed NV centers, Science **366**, 1359 (2019).

[30] T. Wolf, P. Neumann, K. Nakamura, H. Sumiya, T. Ohshima, J. Isoya, and J. Wrachtrup, Subpicotesla diamond magnetometry, Phys. Rev. X **5**, 041001 (2015).

[31] C. Zhang, F. Shagieva, M. Widmann, M. Kübler, V. Vorobyov, P. Kapitanova, E. Nenasheva, R. Corkill, O. Rhrle, K. Nakamura, H. Sumiya, S. Onoda, J. Isoya, and J. Wrachtrup, Diamond magnetometry and gradiometry towards subpicotesla dc field measurement, Phys. Rev. Appl. **15**, 064075 (2021).

[32] K. Chang, A. Eichler, J. Rhensius, L. Lorenzelli, and C. L. Degen, Nanoscale imaging of current density with a single-spin magnetometer, Nano Lett. **17**, 2367 (2017).

[33] J. P. Tetienne, N. Dontschuk, D. A. Broadway, A. Stacey, D. A. Simpson, and L. C. L. Hollenberg, Quantum imaging of current flow in graphene, Sci. Adv. **3**, e1602429 (2017).

[34] A. Nowodzinski, M. Chipaux, L. Toraille, V. Jacques, J. F. Roch, and T. Debuisschert, Nitrogen-vacancy centers in diamond for current imaging at the redistributive layer level of integrated circuits, Microelectron. Reliab. **55**, 1549 (2015).

[35] M. J. Turner, N. Langellier, R. Bainbridge, D. Walters, S. Meesala, T. M. Babinec, P. Kehayias, A. Yacoby, E. Hu, M. Lončar, R. L. Walsworth, and E. V. Levine, Magnetic field fingerprinting of integrated-circuit activity with a quantum diamond microscope, Phys. Rev. Appl. **14**, 014097 (2020).

[36] S. M. Oliver, D. J. Martynowych, M. J. Turner, D. A. Hopper, R. L. Walsworth, and E. V. Levine, in *Conference Proceedings from the International Symposium for Testing and Failure Analysis* (2021), pp. 96–107.

[37] J. Böck, *et al.*, in *Proceedings of the IEEE Bipolar/BiCMOS Circuits and Technology Meeting* (2015), pp. 121–124.

[38] See Supplemental Material http://link.aps.org/supplemental/10.1103/PhysRevApplied.21.014055 for further details about the data analysis procedure, additional simulations regarding overlapping wires in multilayered devices, the definition of the imager's spatial resolution, and a description of a functioning device versus a defective device. The Supplemental Material also contains Refs. [60–78].

[39] B. J. Roth, N. G. Sepulveda, and J. P. Wikswo, Using a magnetometer to image a two-dimensional current distribution, J. Appl. Phys. **65**, 361 (1989).

[40] A. Y. Meltzer, E. Levin, and E. Zeldov, Direct reconstruction of two-dimensional currents in thin films from magnetic-field measurements, Phys. Rev. Appl. **8**, 064030 (2017).

[41] O. Burkacky, M. Patel, N. Sergeant, and C. Thomas, *Reimagining Fabs: Advanced Analytics in Semiconductor Manufacturing* (Copyright © 2017 McKinsey & Company, 2017), pp. 1–7.

[42] D. G. Pierce and P. G. Brusius, Electromigration: A review, Microelectron. Reliab. **37**, 1053 (1997).

[43] N. Singh, A. F. Bower, and S. Shankar, A three-dimensional model of electromigration and stress induced void nucleation in interconnect structures, Modell. Simul. Mater. Sci. Eng. **18**, 065006 (2010).

[44] H. Ceric and S. Selberherr, Electromigration in submicron interconnect features of integrated circuits, Mater. Sci. Eng. R: Rep. **71**, 53 (2011).

[45] C. M. Bishop, *Pattern Recognition and Machine Learning* (Springer, New York, 2006).

[46] M. Holler, M. Odstrcil, M. Guizar-Sicairos, M. Lebugle, E. Müller, S. Finizio, G. Tinti, C. David, J. Zusman, W. Unglaub, O. Bunk, J. Raabe, A. F. J. Levi, and G. Aeppli, Three-dimensional imaging of integrated circuits with macro- to nanoscale zoom, Nat. Electron. **2**, 464 (2019).

[47] M. Chipaux, L. Toraille, C. Larat, L. Morvan, S. Pezzagna, J. Meijer, and T. Debuisschert, Wide bandwidth instantaneous radio frequency spectrum analyzer based on nitrogen vacancy centers in diamond, Appl. Phys. Lett. **107**, 233502 (2015).

[48] J. Zopes and C. L. Degen, Reconstruction-free quantum sensing of arbitrary waveforms, Phys. Rev. Appl. **12**, 054028 (2019).

[49] F. Ziem, M. Garsi, H. Fedder, and J. Wrachtrup, Quantitative nanoscale MRI with a wide field of view, Sci. Rep. **9**, 12166 (2019).

[50] K. Mizuno, H. Ishiwata, Y. Masuyama, T. Iwasaki, and M. Hatano, Simultaneous wide-field imaging of phase and magnitude of AC magnetic signal using diamond quantum magnetometry, Sci. Rep. **10**, 11611 (2020).

[51] F. Casola, T. Van Der Sar, and A. Yacoby, Probing condensed matter physics with magnetometry based on nitrogen-vacancy centres in diamond, Nat. Rev. Mater. **3**, 17088 (2018).

[52] J. L. Webb, L. Troise, N. W. Hansen, L. F. Frellsen, C. Osterkamp, F. Jelezko, S. Jankuhn, J. Meijer, K. Berg-Sørensen, J. F. Perrier, A. Huck, and U. L. Andersen, High-speed wide-field imaging of microcircuitry using nitrogen vacancies in diamond, Phys. Rev. Appl. **17**, 064051 (2022).

[53] M. Parashar, A. Bathla, D. Shishir, A. Gokhale, S. Bandyopadhyay, and K. Saha, Sub-second temporal magnetic field microscopy using quantum defects in diamond, Sci. Rep. **12**, 8743 (2022).

[54] G. J. Abrahams, S. C. Scholten, A. J. Healey, I. O. Robertson, N. Dontschuk, S. Q. Lim, B. C. Johnson, D. A. Simpson, L. C. L. Hollenberg, and J. P. Tetienne, An integrated widefield probe for practical diamond nitrogen-vacancy microscopy, Appl. Phys. Lett. **119**, 254002 (2021).

[55] L. Toraille, A. Hilberer, T. Plisson, M. Lesik, M. Chipaux, B. Vindolet, C. Pépin, F. Occelli, M. Schmidt, T. Debuisschert, N. Guignot, J. P. Itié, P. Loubeyre, and J. F. Roch, Combined synchrotron x-ray diffraction and NV diamond magnetic microscopy measurements at high pressure, New J. Phys. **22**, 103063 (2020).

[56] N. Courjault, F. Infante, V. Bley, T. Lebey, and P. Perdu, in *Proceedings of the 21th International Symposium on the Physical and Failure Analysis of Integrated Circuits (IPFA)* (2014), pp. 26–29.

[57] H. H. Eroğlu, O. Puonti, C. Göksu, F. Gregersen, H. R. Siebner, L. G. Hanson, and A. Thielscher, On the reconstruction of magnetic resonance current density images of the human brain: Pitfalls and perspectives, Neuroimage **243**, 118517 (2021).

[58] B. J. Yang, E. G. Moon, H. Isobe, and N. Nagaosa, Quantum criticality of topological phase transitions in three-dimensional interacting electronic systems, Nat. Phys. **10**, 774 (2014).

[59] C. Wang, A. C. Potter, and T. Senthil, Classification of interacting electronic topological insulators in three dimensions, Science **343**, 629 (2014).

[60] J. Mistrik, S. Kasap, H. E. Ruda, C. Koughia, and J. Singh, Optical properties of electronic materials: Fundamentals and characterization, in *Springer Handbook of Electronic and Photonic Materials*, edited by S. Kasap and P. Capper (Springer, Cham, 2017), pp. 47–83.

[61] F. J. Zeleznik, Quasi-Newton methods for nonlinear equations, J. Assoc. Comput. Mach. **15**, 265 (1968).

[62] K. Levenberg, A method for the solution of certain non-linear problems in least squares, Q. Appl. Math. **2**, 164 (1944).

[63] D. W. Marquardt, An algorithm for least-squares estimation of nonlinear parameters, J. Soc. Ind. Appl. Math. **11**, 431 (1963).

[64] A. Dréau, M. Lesik, L. Rondin, P. Spinicelli, O. Arcizet, J. F. Roch, and V. Jacques, Avoiding power broadening in optically detected magnetic resonance of single NV defects for enhanced dc magnetic field sensitivity, Phys. Rev. B **84**, 195204 (2011).

[65] P. Udvarhelyi, V. O. Shkolnikov, A. Gali, G. Burkard, and A. Pályi, Spin-strain interaction in nitrogen-vacancy centers in diamond, Phys. Rev. B **98**, 075201 (2018).

[66] V. M. Acosta, E. Bauch, M. P. Ledbetter, A. Waxman, L. S. Bouchard, and D. Budker, Temperature dependence of the nitrogen-vacancy magnetic resonance in diamond, Phys. Rev. Lett. **104**, 070801 (2010).

[67] M. W. Doherty, V. M. Acosta, A. Jarmola, M. S. J. Barson, N. B. Manson, D. Budker, and L. C. L. Hollenberg, Temperature shifts of the resonances of the NV-center in diamond, Phys. Rev. B: Condens Matter Mater. Phys. **90**, 041201 (2014).

[68] F. Dolde, H. Fedder, M. W. Doherty, T. Nöbauer, F. Rempp, G. Balasubramanian, T. Wolf, F. Reinhard, L. C. L. Hollenberg, F. Jelezko, and J. Wrachtrup, Electric-field sensing using single diamond spins, Nat. Phys. **7**, 459 (2011).

[69] D. A. Broadway, N. Dontschuk, A. Tsai, S. E. Lillie, C. T. K. Lew, J. C. McCallum, B. C. Johnson, M. W. Doherty, A. Stacey, L. C. L. Hollenberg, and J. P. Tetienne, Spatial mapping of band bending in semiconductor devices using in situ quantum sensors, Nat. Electron. **1**, 502 (2018).

[70] Y. Schlussel, T. Lenz, D. Rohner, Y. Bar-Haim, L. Bougas, D. Groswasser, M. Kieschnick, E. Rozenberg, L. Thiel, A. Waxman, J. Meijer, P. Maletinsky, D. Budker, and R. Folman, Wide-field imaging of superconductor vortices with electron spins in diamond, Phys. Rev. Appl. **10**, 034032 (2018).

[71] C. R. Goodall, Computation using the QR decomposition, in *Handbook of Statistics 9: Computational Statistics*,

edited by C. R. Rao (Elsevier, Amsterdam, 1993), pp. 467–501.

[72] A. Chambolle, An algorithm for total variation minimization and applications, J. Math. Imaging Vis. **20**, 89 (2004).

[73] D. A. Broadway, S. E. Lillie, S. C. Scholten, D. Rohner, N. Dontschuk, P. Maletinsky, J.-P. Tetienne, and L. C. L. Hollenberg, Improved current density and magnetization reconstruction through vector magnetic field measurements, Phys. Rev. Appl. **14**, 024076 (2020).

[74] J. W. S. X. V. Rayleigh, On the theory of optical images, with special reference to the microscope, London, Edinburgh Dublin Philos. Mag. J. Sci. **42**, 167 (1896).

[75] Beyond the diffraction limit, Nat. Photonics **3**, 361 (2009).

[76] M. Pfender, N. Aslam, G. Waldherr, P. Neumann, and J. Wrachtrup, Single-spin stochastic optical reconstruction microscopy, Proc. Natl. Acad. Sci. USA **111**, 14669 (2014).

[77] C. M. Sparrow, On spectroscopic resolving power, Astrophys. J. **44**, 76 (1916).

[78] T. Yu, H. Liu, and W. Cai, On the quantification of spatial resolution for three-dimensional computed tomography of chemiluminescence, Opt. Express **25**, 24093 (2017).